Micro-optical coherence tomography for high-resolution morphologic imaging of cellular and nerval corneal micro-structures

ANDREAS WARTAK,[1,2,7] 🆔 MERLE S. SCHENK,[1,3,7] VERENA BÜHLER,[1,4] STEFAN A. KASSUMEH,[1,3] REGINALD BIRNGRUBER,[1,4,8] AND GUILLERMO J. TEARNEY[1,5,6,8,*]

[1]*Wellman Center for Photomedicine, Massachusetts General Hospital, Boston, MA 02114, USA*
[2]*Department of Dermatology, Harvard Medical School, Harvard University, Boston, MA 02115, USA*
[3]*Department of Ophthalmology, University Hospital, LMU Munich, Munich 80336, Germany*
[4]*Institute of Biomedical Optics, University of Lübeck, Lübeck 23562, Germany*
[5]*Department of Pathology, Massachusetts General Hospital, Harvard Medical School, Boston, MA 02114, USA*
[6]*Harvard-MIT Division of Health Sciences and Technology, Cambridge, MA 02139, USA*
[7]*co-first authors*
[8]*co-senior authors*
[*]*gtearney@partners.org*

Abstract: We demonstrate the highest resolution (1.5×1.5×1 μm) micrometer optical coherence tomography (μOCT) imaging of the morphologic micro-structure of excised swine and non-human primate corneas. Besides epithelial, stromal, and endothelial cell morphology, this report focuses on investigating the most peripheral corneal nerve fibers, the nerve fibers of the subbasal plexus (SBP). Alterations of SBP nerve density and composition are reportedly linked to major neurologic disorders, such as diabetic neuropathy, potentially indicating earliest onsets of denervation. Here, the fine, hyperreflective, epithelial nerve structures located just above Bowman's membrane, are i) visualized using our μOCT prototype, ii) validated by comparison to fluorescence confocal microscopy (including selective immunohistochemical staining), and iii) segmented using state-of-the-art image processing. Here, we also introduce polarization sensitive (PS) μOCT imaging, demonstrating, to the best of our knowledge, the highest resolution corneal PS-OCT scans reported to date.

1. Introduction

The cornea is one of the most densely innervated tissues of the human body [1]. All nerves innervating the corneal stroma and epithelium are branches of the ophthalmic division of the trigeminal nerve [1–3]. Commonly, the nerval network within the cornea is divided into three plexi in planes parallel to the corneal surface: i) the stromal plexus (STP), ii) the subepithelial plexi (SEP), and iii) the subbasal plexus (SBP) [1–4]. The STP is home to the large diameter nerves that enter the cornea from the limbus and branch out to eventually give rise to the smaller diameter fiber networks of the SEP and the SBP. The SEP forms in the anterior stroma below Bowman's membrane (BM), which separates the corneal stroma from the epithelium. Some of its finer branches pierce through BM, thus forming the SBP, located above BM at the interface to the basal epithelial cell layers. The SBP consists of long delicate bundles that approach the apex from the periphery, before either crossing it (6-12 hr. direction) or circling back towards the periphery (5-1, 7-11, 4-2, 8-10 hr. direction) [1]. The SBP extends exclusively within a single plane parallel to the corneal surface with some terminal nerve endings branching perpendicular towards the corneal surface. Being the finest and most peripheral of the three described plexi

(typical nerve diameters between 0.1 and 0.5 μm [1]), the SBP is considered most prone to experiencing pathological transformations manifesting as incipient denervation [1,3].

While corneal nerves are known for their importance for corneal wound healing, the blink reflex, and tear production, as well as for sensory and thermal perception [1], they have also been reported to inform on the systemic innervation status of the human body as a whole. Due to its easy accessibility and optical transparency, the cornea is regarded a window to the peripheral nervous system, enabling to spot the earliest onsets of nerval degeneration in a range of systemic diseases [5–7], that cannot be observed elsewhere. Thus, there exists a clear clinical interest to visualize these μm and sub-μm thin nerve fiber structures of the SBP for assessing early signs peripheral neuropathy.

Besides some electron microscopy reports [8,9], corneal nerve morphology has usually been studied using optical imaging means, often in combination with immunohistochemistry [10,11]. The first modality to enable corneal subbasal nerve imaging in living eyes was *in vivo* confocal microscopy (IVCM) [2,12–14]. Due to its impressive image quality in terms of contrast and resolution, this commercially available technology has already established itself as the standard for corneal nerve imaging *in vivo*. Besides purely ophthalmic investigations, IVCM's capability to visualize small fractions of the SBP has triggered numerous clinical studies regarding various systemic neurologic disorders. Alterations in subbasal nerve density have been reported in studies of diabetic and Parkinson's disease patients [5,7], as well as people suffering from certain autoimmune and genetic disorders [3,6]. IVCM nonetheless has several shortcomings that impede utility in daily clinical practice: First, it is a contact imaging modality, requiring anesthetics and constant physical contact between the instrument's end cap and the subject's cornea, causing patient discomfort. Second, it is a single plane imaging modality, and thus highly sensitive to subject motion. Third, it uses high numerical aperture (NA) objectives, generally limiting the field-of-view (FOV) to a maximum of 400×400 μm.

Besides recently introduced retroillumination microscopy [15], a different optical imaging modality that enables SBP visualization in humans *in vivo*, is optical coherence tomography (OCT) [16–18]. Even though OCT offers high-speed (large FOV), depth-resolved, non-contact imaging, conventional commercial OCT lacks the transverse resolution (typically ~15-25 μm) as well as the axial sectioning capabilities (typically ~7-10 μm) to resolve peripheral corneal nerve structures. However, technological OCT advances such as ultrahigh-resolution (UHR-) OCT [19–21], full-field (FF-) OCT [22–25], micrometer (μ-) OCT [26–28], or Gabor-domain (GD-) OCT [29,30] have been demonstrated to improve imaging resolutions by roughly an order of magnitude in every dimension, thus enabling visualization of subbasal corneal nerves.

In this paper we present highest resolution μOCT imaging results of swine and non-human primate corneas (which are known to accommodate very similar network structures to human corneal nerves), *ex vivo*, at close to isotropic voxel resolutions of 1.5×1.5×1 μm. In particular, we demonstrate imaging of the SBP and introduce a processing pipeline towards quantitative nerve density evaluation. We correlate and validate the nerval origin of the tracked fiber structures using a selective immunohistochemical staining approach. In addition, we present, to the best of our knowledge, first corneal PS-μOCT image data, providing tissue-specific contrast that may be complementary to purely morphologic imaging.

2. Methods

2.1. Imaging

The μOCT bench-top prototype employed in this study (Fig. 1) uses a conventional bulk-optic Michelson interferometer based spectral domain (SD-) OCT approach incorporating a supercontinuum light source (NKT Photonics, Inc., Denmark) for broadband illumination (650-950 nm) as well as a high-speed (70 kHz) 8192 pixel line camera (Emergent Vision Technologies, USA) for increased spectral resolution detection. Volumetric μOCT image data was recorded

over field-of-views (FOV) ranging from 500×500 µm to 1000×1000 µm at sampling densities of 500×500 to 1000×1000 pixels, resulting in acquisition times of 3.5 to 14.3 s at line scan rate of 70 kHz. At illumination powers of 10-20 mW on the sample, the sensitivity of the instrument ranged between 90-93 dB, with a 5-6 dB roll-off per mm over a depth range of 4.5 mm. In order to allow for close to isotropic voxel resolution imaging, a NIR infinity corrected 0.4 NA plan-apochromat (Mitutoyo, Japan) was employed as the objective. To match sample and reference arm dispersion, the same objective was also incorporated in the reference arm of the instrument. Thus, a transverse resolution of ~1.5 µm was achieved (over a Rayleigh range of ~15 µm), which is close to the system's axial resolution of just below 1 µm in corneal tissue (n = 1.37).
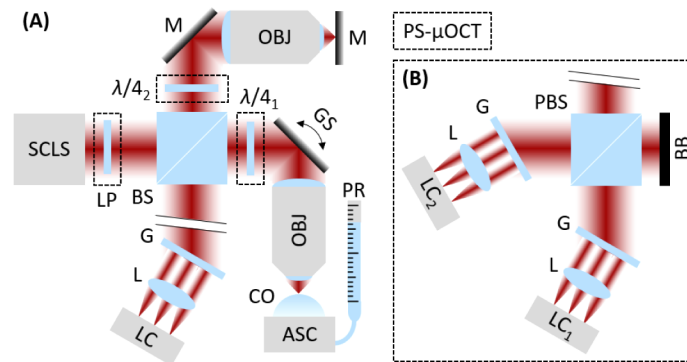
Fig. 1. Simplified schematics of (PS-) µOCT imaging prototypes. (A) Bulk-optics Michelson interferometer with source, sample, reference, and detection arm. Additional components for PS imaging mode framed with dashed lines. (B) Polarization sensitive detection unit including two identical spectrometer units for PS imaging mode. SCLS – supercontinuum light source, LP – linear polarizer, BS – bulk-optic beam splitter, $\lambda/4_1$ – quarter wave plate at 45°, GS – 2D galvo scanner, OBJ – plan-apochromat objective, CO – cornea, ASC – anterior segment chamber, PR – pressure reservoir, $\lambda/4_2$ – quarter wave plate at 22.5°, M – mirror, G – diffraction grating, L – lens, LC – line camera, PBS – bulk-optic polarizing beam splitter, BB – beam block.

The instrument is also capable of polarization sensitive µOCT imaging by introducing a polarizing beam splitter and a second identical spectrometer unit in the detection arm of the interferometer (Fig. 1(B)) [31]. A single-input state PS-OCT scheme was implemented using a polarizer before the beam splitter and a $\lambda/4$-waveplate in both the sample and reference arms [32]. In the sample arm, the linear input state was converted to circularly polarized light at the sample by orienting the $\lambda/4$-waveplate at 45°, while the $\lambda/4$-waveplate in the reference arm was oriented at 22.5° to allow for 45° linear polarized light in the polarization sensitive detection unit.

Fluorescence confocal microscopy (FCM) of βIII-tubulin-stained corneas was performed using a commercial automated laser scanning FCM (Olympus, Japan) at 635 nm excitation and detection from 660 to 735 nm. A 60x objective (1.2 NA) was employed to allow for high transverse resolution FCM imaging.

2.2. Sample preparation and immunohistochemistry

Within this study, excised eyes of mature swine (Yorkshire/Landrace hybrid) and non-human primates (Cynomolgus macaques) were imaged. All study procedures were approved by the Institutional Animal Care and Use Committee (IACUC, exempt ID: 2019N000082 and 2018N000214) at the Massachusetts General Hospital (MGH, USA). Corneal µOCT imaging of the cadaver globes was performed within 1 to 3 hrs. of the respective animal's death. Either

a whole-eye mount or an anterior segment chamber (for corneo-scleral discs only) were used in addition to a pressure reservoir for intraocular pressure control (18 mmHg) to enable near physiologic imaging conditions. For the whole-eye mount, a 14-gauge hollow needle was used to pierce into the vitreous from posterior, while the anterior segment mount was constructed to allow for a constant pressurized artificial anterior segment chamber that was sealed-off anteriorly by the corneal disc itself. Between recordings, the eyes/corneo-scleral discs were kept moist with a 20% w/v dextran solution to avoid surface desiccation, while for transport before and after µOCT imaging they were kept in phosphate-buffered saline (PBS).

Immunohistochemical staining of the corneal nerve structures was achieved using a βIII-tubulin antibody staining protocol [33], adapted for swine and non-human primate corneas. A detailed description of the entire histochemical staining procedure can be found elsewhere [34]. Each cornea was placed onto a microscopy slide and secured using a cover slip before FCM imaging.

2.3. Data processing and analysis

Standard SD-OCT pre-processing (background subtraction, λ-k remapping, numerical dispersion compensation, Fourier transformation) was performed on the raw spectral fringe (PS-) µOCT data sets. In addition to conventional intensity tomograms, polarization sensitive contrast (phase retardation, squared intensity, and additive color ratio images) was derived from the same data sets, following previously described processing steps for single-input state PS-OCT [32].

Field-distortions introduced by the imaging setup in addition to the highly convex curvature of the mounted cornea complicate matching of the focus plane with a corneal plane of interest. Thus, in order to obtain *en face* projections of a specific corneal layer, post-processing image segmentation was performed (Fig. 2). An automatic 2D graph-based retinal layer segmentation method for posterior ophthalmic OCT imaging, described in previously published work [35],
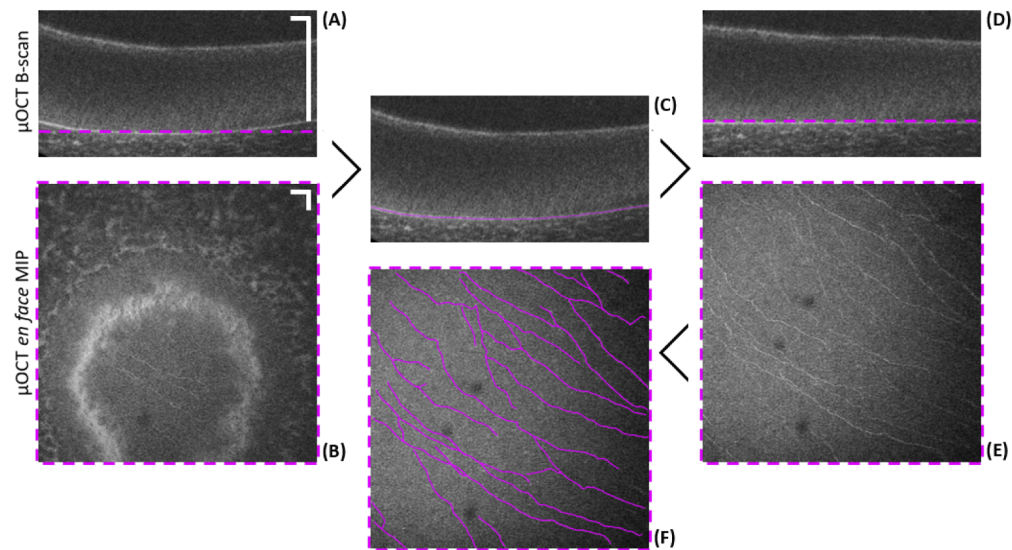
Fig. 2. Illustration of image segmentation procedure to extract the SBP in a volumetric µOCT scan of a swine cornea. (A) Unsegmented B-scan of corneal epithelium. (B) Unsegmented *en face* MIP over ~3 µm in depth at BM. Only a small fraction of the FOV visualizes the SBP. (C) Same B-scan as in (A) with the indicated segmentation line of BM. (D) B-scan segmented and flattened in accordance to the segmentation line. (E) Segmented *en face* MIP over ~3 µm in depth just above BM. Entire FOV visualizes the SBP. (F) Results of semiautomatic nerve tracking procedure on the *en face* MIP of (E). Scale bars: 50 µm.

was adapted (using MATLAB (The MathWorks Inc., USA)) for segmentation of the BM in every B-scan of the volumetric data set (Fig. 2(C)). In a final step, flattening of the segmented plane was performed by independent A-scan axial pixel shifts towards the reference plane. Figure 2 depicts exemplary image data of a swine cornea that illustrates the advantage of using this segmentation algorithm for visualization of single cell layers within the 3D data set. Figure 2(A) and (B) show a B-scan and an *en face* maximum intensity projection (MIP) over a depth of ∼3 µm of the unsegmented data set, respectively, while Fig. 2(D) and (E) show the same B-scan and *en face* projection after segmentation.

Regarding the generation of nerve density maps (Fig. 2(F)), nerve skeletonization of the subbasal plexus was performed via semiautomatic nerve tracking using the ImageJ [36] software plugin NeuronJ [37].

3. Results

Figure 3 depicts exemplary morphologic µOCT imaging results of all major corneal compartments (epithelium, stroma, and endothelium) of an excised non-human primate cornea in different imaging planes – the cross-sectional plane (Figs. 3(A, B)) and the *en face* plane (Figs. 3(C, D)), respectively. Figures 3(A, B) illustrate a comparison of two different objective lenses resulting in a completely different depth-of-field (DOF), and hence transverse resolution. For Fig. 3(A) a simple 25 mm achromat doublet was used as objective lens, while for Fig. 3(B) the previously discussed 0.4 NA microscope objective was employed. In Fig. 3(A) the DOF is large enough to provide decent signal throughout the entire corneal thickness (here ∼400 µm), enabling visualization of epithelium, Bowman's membrane, stroma, Descemet's membrane, and endothelium in a single B-scan. In contrast, Fig. 3(B) provides separately acquired B-scan images of the epithelial and the endothelial region, respectively, stitched together at a significantly decreased DOF. The enhanced signal fall-off over depth resulting from the greatly reduced DOF with the higher NA objective is apparent in both the epithelial and endothelial section. Figure 3(C) provides an illustration of a stacked *en face* MIP (∼3 µm in depth; area of 700×700 µm), presented in greater detail in Fig. 3(D). These projections depict cellular and nerval morphology details of epithelial, stromal, and endothelial layers. In particular, the following layers are depicted: i) squamous epithelial cells, ii) superficial epithelial cells, iii) intermediate epithelial wing cells, iv) anterior basal epithelial cells, v) posterior basal epithelial cells, vi) terminal nerve endings, vii) subbasal nerve plexus (SBP), viii) Bowman's membrane, ix) anterior stroma, x) midstromal nerves, xi) posterior stroma, xii) endothelial cells. In the squamous epithelial cell layer, highly scattering cell nuclei can be observed, while in the superficial and intermediate epithelial cell layers, high-contrast membranes of the large epithelial cells are observed. The highly scattering cell membranes are also observed in the basal cell layers where the cells decrease in size towards the BM. The panel labeled 'terminal nerve endings' shows several hyperreflective dots and first signs of small winding longitudinal structures, that the authors consider to be part of the most peripheral terminal nerve endings. The SBP shows a multitude of fine, highly scattering subbasal nerves, while the acellular BM presents as a more or less homogeneously hyperreflective, featureless layer. Different shapes of highly scattering keratocytes are observed in the anterior, mid, and posterior stroma, respectively. Large stromal nerves visualized as bright linear structures that branch frequently are encountered throughout the entire stromal thickness. Finally, the endothelial cells interestingly present with low scattering cell membranes as well as cell nuclei, but highly scattering cytoplasm. Multiple cycles of focus adjustment in *z* were necessary to map all presented *en face* images throughout the entire corneal thickness at highest transverse resolution.

To demonstrate that our µOCT prototype can visualize the SBP reproducibly, multiple corneas of two species (swine, non-human primate) were imaged (Fig. 2–4). The nerval origin of the hyperreflective structures was confirmed by FCM images acquired from the same corneas.
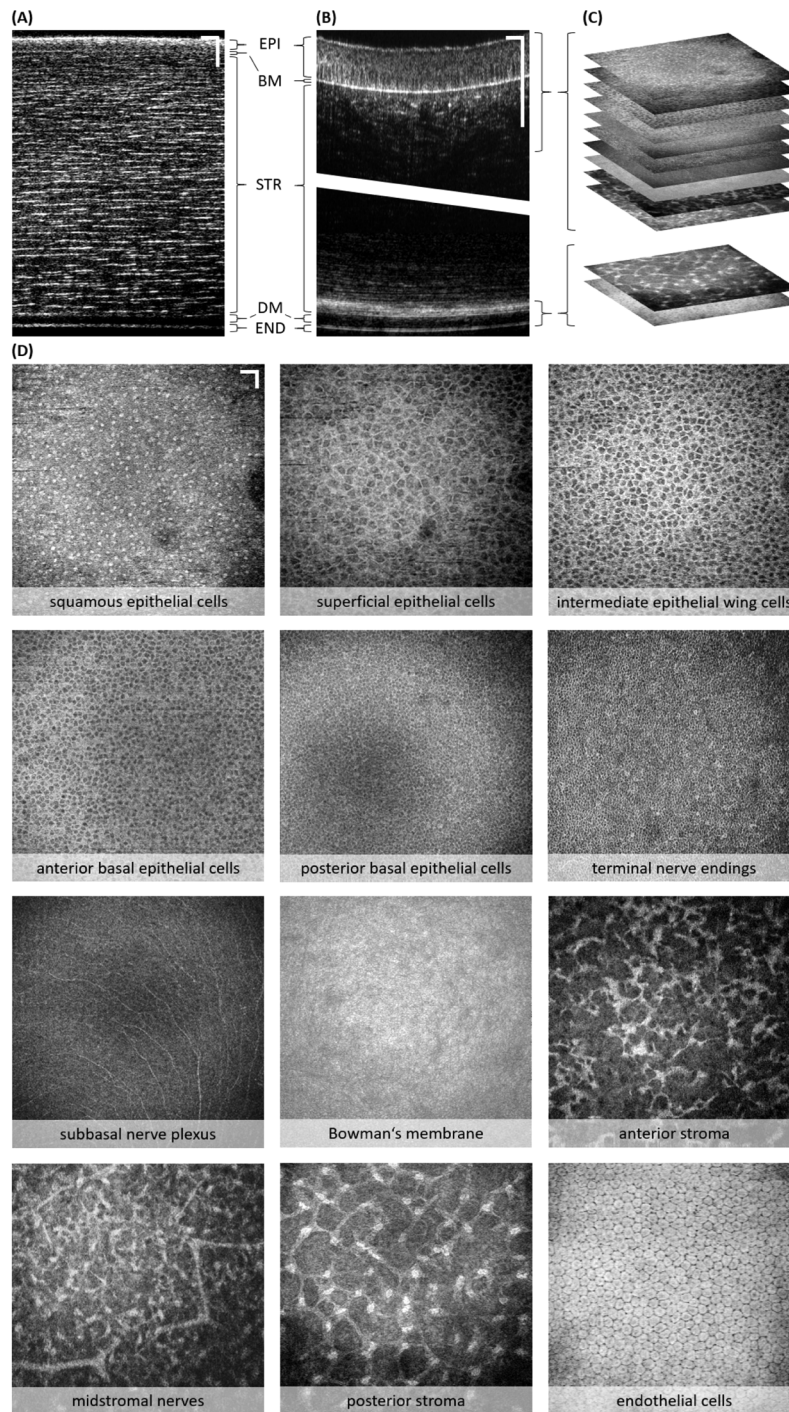
Fig. 3. Cellular and nerval morphology of epithelial, stromal, and endothelial corneal layers of an excised non-human primate cornea. (A) B-scan of entire corneal thickness (∼400 µm) acquired using a low NA objective lens. Corneal layers indicated: EPI – epithelium, BM – Bowman's membrane, STR – stroma, DM – Descemet's membrane, END – endothelium. (B) B-scans of epithelial and endothelial region acquired using high NA objective (stitched together to allow for comparison to (A); vertical scales of (A) and (B) do not match). (C) Illustration of multiple *en face* MIP of different depth layers computed from the 3D data set. (D) *En face* MIP over ∼3 µm in depth of twelve specific corneal layers. Scale bars: 50 µm.

Figure 4 presents exemplary image data of a respective SBPs from a non-human primate cornea. From left to right (Fig. 4(A)-(D)) the μOCT SBP plane *en face* MIP (~3 μm in depth; area of 700×700 μm) is followed by the overlaid results of the semi-automatic nerve tracking (magenta), which is followed by the binary skeletonization masks of the tracked nerve structures (magenta and black), which is again followed by FCM images that was not locally matched to the μOCT images, but presents with similar appearance. The representative data set depicts a homogenous linear striped nerve pattern as observed in most imaged corneas.
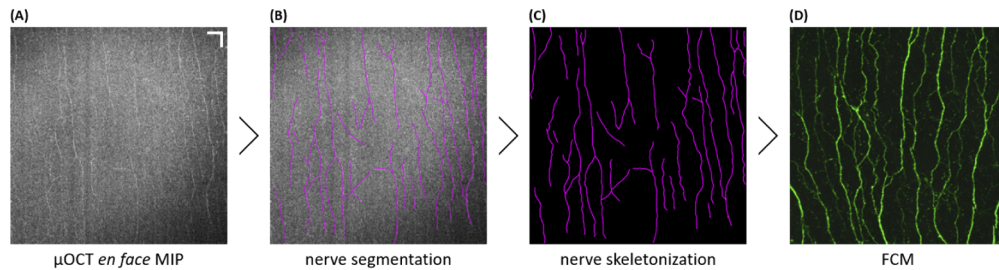

Fig. 4. Comparison of SBP nerve morphology between μOCT and FCM. (A) *En face* μOCT, (B) semi-automatic nerve tracking (magenta), (C) binary nerve skeletonization (magenta and black), (D) and FCM image of a non-human primate cornea. Scale bars: 50 μm.

The nerve tracking/skeletonization enables computation of image metrics such as *number of traces*, *individual* and *mean trace length*, and *nerve density* (ratio of image pixels of the entire FOV occupied by nerve traces), thus allowing for quantitative evaluation of the innervation status. However, this evaluation is not within the scope of this manuscript.

Exemplary image data of first PS-μOCT investigations are presented in Figs. 5 and 6. Cross-sectional plane, Figs. 5(A)-(D), and transverse plane images, Figs. 5(F)-(I) and Figs. 6(A)-(F), of the anterior part (posterior epithelium, BM, anterior stroma) of an excised non-human primate cornea are depicted in intensity as well as polarization contrast (phase retardation and additive color ratio). Figures 5(A)-(C) depict unsegmented co-, cross-polarized and squared intensity B-scans, respectively, clearly indicating differences in epithelial and stromal visualization. Figure 5(D) employs a phase retardation image to quantify the polarization changes that are mainly attributed to the birefringent properties of the corneal stroma. The ROI in Fig. 5(D) is magnified in Fig. 5(E), allowing clear differentiation between the posterior epithelium, BM, and the anterior stroma. Figure 5(F) and (G) present unsegmented *en face* MIP (~3 μm in depth; area of 800×800 μm) of the co- and cross-polarized channel, respectively. The projection cuts through the posterior epithelium, BM, and the anterior stroma, exposing striking differences in the appearance of structural features. To provide an improved comparison, both, co- and cross-polarized data sets were segmented using the previously discussed BM layer segmentation algorithm. Figures 5(H) and (I) present segmentation results for both channels of the corneal stroma just beneath BM. In order to facilitate a direct comparison of both the co- and cross-polarized channel images, the additive color ratio was computed after coloring the corresponding *en face* MIPs in complementary colors (co-polarized in green; cross-polarized in magenta). While image features that only appear in one of the two images are visualized in their respective color, those image features appearing in both images at similar intensity appear white. Figures 6(A)-(F) depict such additive color ratio images of the anterior stroma, the most anterior stroma, the border area between stroma and BM, the anterior BM, and the subbasal nerve plexus (SBP).
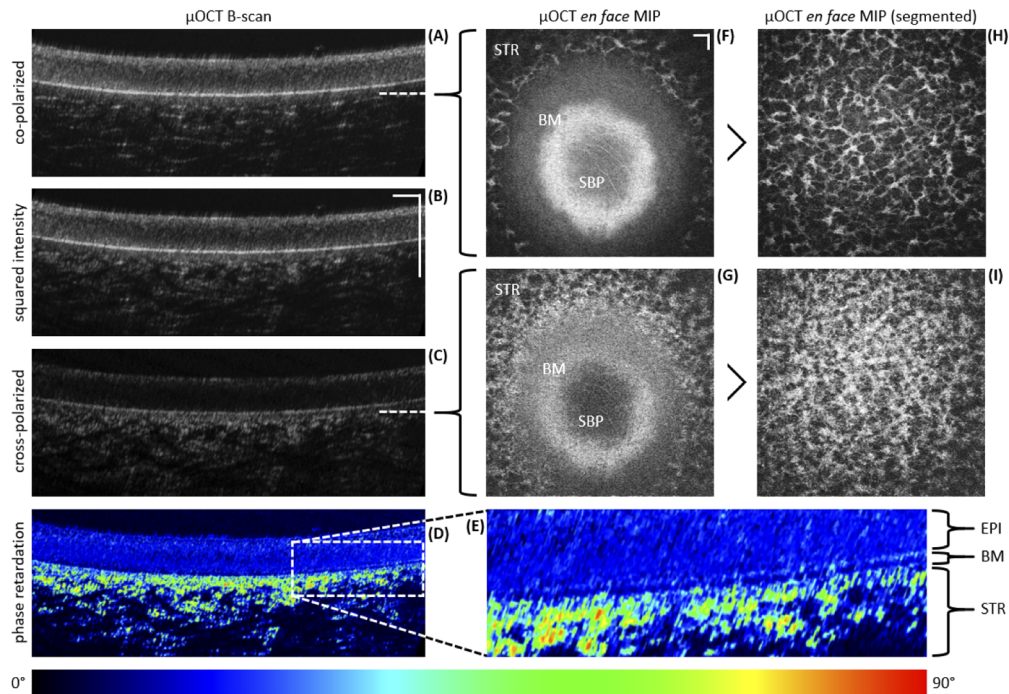
Fig. 5. Anterior corneal PS-µOCT image data of an excised non-human primate cornea. (A)-(E) Intensity and phase retardation tomograms. (F)-(I) Intensity *en face* MIP of unsegmented and segmented epithelial and stromal layers (over ~3 µm in depth). Co-polarized (A), cross-polarized (C), and squared intensity (B) B-scans. Phase retardation B-scan (D) and magnified ROI (E), highlighting boundaries between the epithelium (EPI), Bowman's membrane (BM), and stroma (STR). Unsegmented co-polarized (F) and cross-polarized (G) *en face* MIP through the subbasal nerve plexus (SBP), Bowman's membrane (BM), and the anterior stroma (STR). Segmented co-polarized (H) and cross-polarized (I) *en face* MIP of the most anterior stroma. Scale bars: 50 µm.
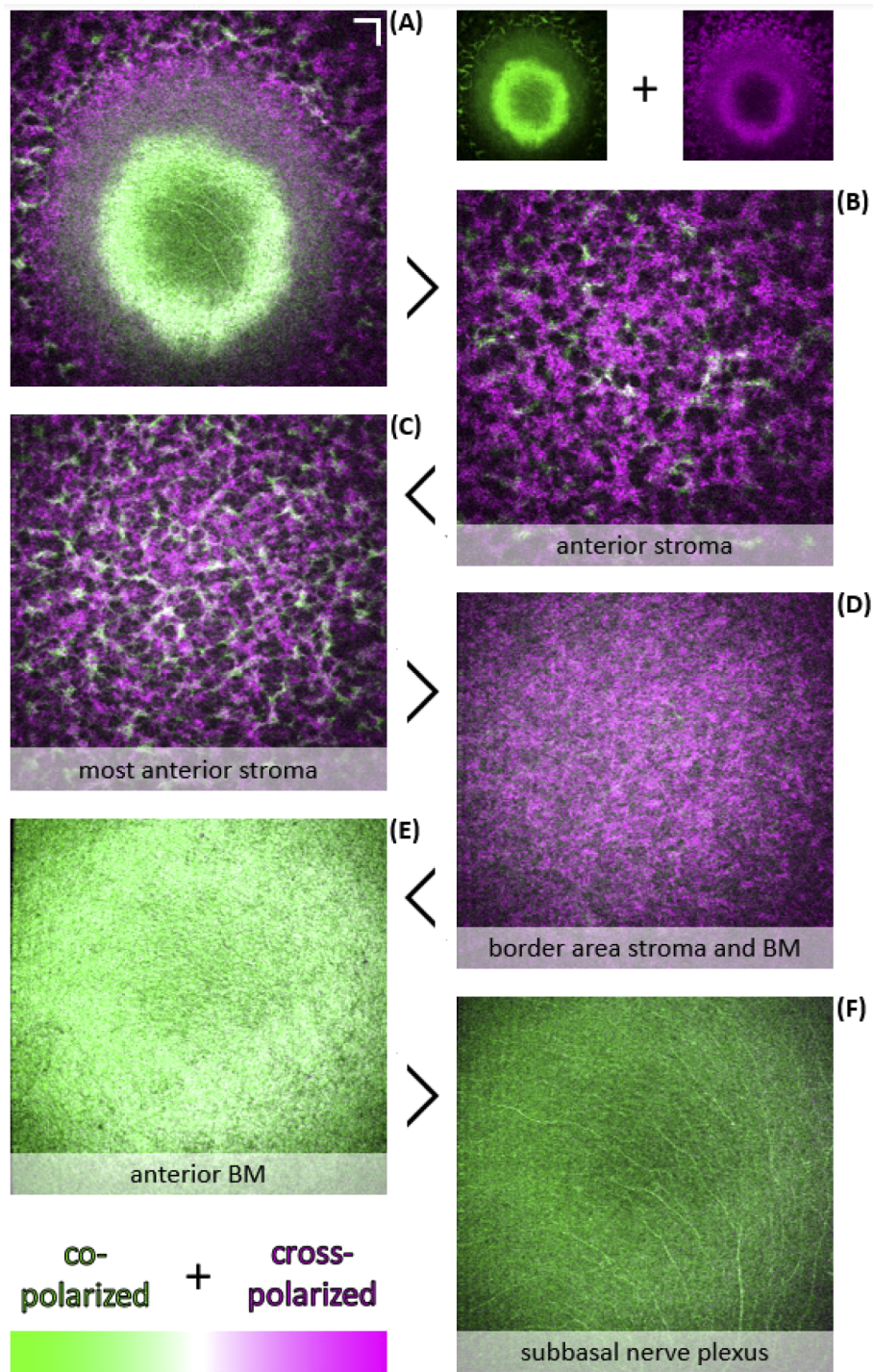
Fig. 6. Anterior corneal PS-µOCT image data of an excised non-human primate cornea. (A)-(F) Additive color ratio *en face* MIP of the anterior stroma, BM, and the posterior epithelium (over ~3 µm in depth). (A) Unsegmented additive color ratio *en face* MIP of Figs. 5(F) and (G). Anterior stroma (B), most anterior stroma (C), border area between stroma and BM (D), BM (E), and subbasal nerve plexus (SBP) (F) additive color ratio images (co-polarized in green; cross-polarized in magenta; areas of similar intensity result in white). Scale bars: 50 µm.

4.   Discussion

From a purely imaging point of view IVCM is sufficient for corneal morphology visualization. Its image quality is outstanding in both contrast and resolution [2,12–14]. Nevertheless, IVCM is not routinely used in daily clinical practice due to its three critical shortcomings: contact modality, single plane imaging, and limited FOV. Our μOCT corneal imaging results on the other hand, were acquired contact-free, were depth-resolved, and had roughly 4 times the FOV. In addition, the beneficial decoupling of axial and transverse imaging resolutions in μOCT allows for increased axial sectioning capabilities in comparison to IVCM (~1 μm vs. ~7 μm). In terms of image quality μOCT is near that of IVCM, although it falls a bit short on resolution due to its lower NA (0.4 vs. 0.8). Nevertheless, the advantages of high-resolution OCT for corneal morphologic imaging suggest that it might be more convenient for clinical use than IVCM [16–18,20,23–25,28,30].

Here, we demonstrated that μOCT can visualize the fine nerve structures of the SBP, commonly referred to as the initial corneal nerve plexus, that experience alterations in disease. Quantification of such alterations is of utmost importance for clinicians in order to detect a potential pathology and grade its severity. This task requires computational assistance in the form of automatic image segmentation and analysis [18]. In this paper, we introduce a processing pipeline towards quantitative nerve density evaluation that combines an automatic layer segmentation and a semi-automatic nerve tracking algorithm. Even though we only present proof-of-concept results here, we emphasize the importance of quantification towards a potential future clinical biomarker, such as the described *nerve density* value.

Besides subbasal nerve imaging, we presented image data of the posterior part of the posterior basal cell layer that comprises several hyperreflective dots and first signs of small winding longitudinal structures (Fig. 3(D)). We consider these structures to potentially be a part of the terminal nerve endings that are known to pierce through this layer towards more anterior epithelial cell layers [1–3]. Since we have not observed similar structures in more anterior layers, we assume that we are only visualizing the largest diameter terminal nerve endings before they thin out anteriorly. Although, this claim is difficult to prove without direct matching FCM comparison, we have observed similar features in multiple corneas (Fig. 7). Figure 7(A) displays the same posterior basal cell layer already presented in Fig. 3(D), and Fig. 7(B) displays an additional similar image from another non-human primate cornea. In both panels, regions of interest (ROI) are magnified and framed in different colors (magenta, green, cyan) while colored arrow heads point to the respective hyperreflective features. The white arrow heads in Fig. 7(B) indicate stripe artefacts due to imperfect layer segmentation. If our assumption is correct, this would be the first visualization of the most peripheral corneal nerve structures, the terminal nerve endings, using OCT.

The polarization properties of the cornea have been analyzed in great detail in previous PS-OCT studies [31,38]. It has been reported, that the corneal epithelium and BM show polarization preserving properties [39], while the corneal stroma is highly birefringent due to its collagen lamellae structure [39,40]. Here, we presented first volumetric highest resolution PS-μOCT corneal imaging results in Figs. 5 and 6. Cross-sectional retardation images (Fig. 5(D) and (E)), demonstrate improved visualization of the posterior boundary of BM, thus potentially enabling highly accurate thickness measurements of BM [41]. The additive color ratio images provide a means to compare structural features between both polarization channels, qualitatively. Figure 6(A) depicts an unsegmented *en face* MIP by combining Figs. 5(F) and (G), and Figs. 6(B)-(F) depict five segmented layers in proximity to BM. The anterior stroma (Fig. 6(B)) is dominated by features from the cross-polarized channel (magenta), while features from the co-polarized channel (green) increase in density towards BM (Fig. 6(C)). Interestingly, the features in both polarization channels differ strikingly in shape and appearance, especially in the most anterior stroma as is apparent in Figs. 5(H) and (I). In the co-polarized image, the fine features of the
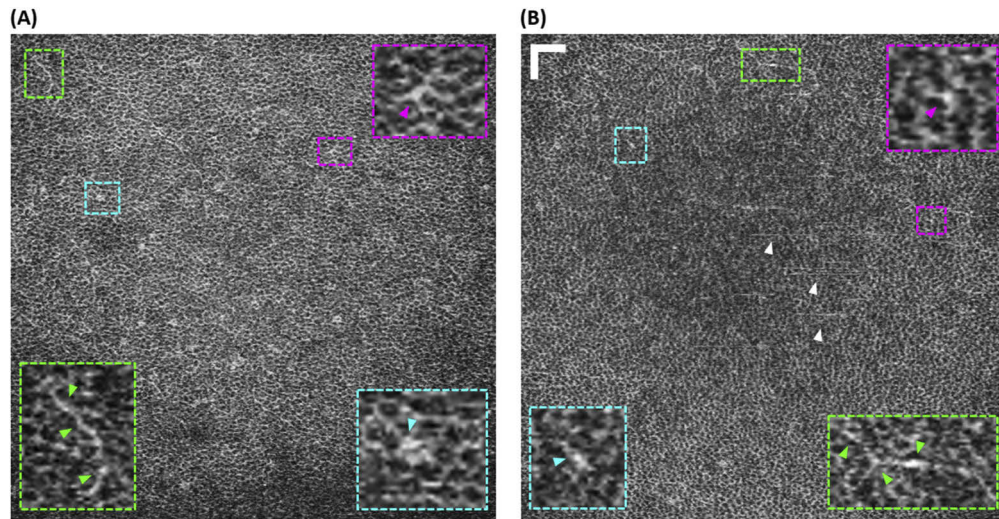
Fig. 7. Potential terminal nerve endings in posterior basal cell layer in excised non-human primate corneas. (A) Same image depicted in Fig. 3(D). (B) Image from a different cornea (white arrow heads indicate stripe artifacts due to imperfect layer segmentation). Both panels depict magnified ROIs of hyperreflective image features that are denoted by arrow heads in the respective colors. The green ROIs display short, thin, longitudinally winding structures similar in appearance to subbasal nerves. The magenta and cyan ROIs depict hyperreflective dots that potentially resemble cross-sections of the terminal nerve endings piercing trough the basal cell layer, commonly in the border area between adjacent basal cells. Scale bars: 50 µm.

keratocyte and nerve network present with sharp image contrast and high resolution, whereas the cross-polarized image shows much more granular structures at lower contrast and seemingly lower transverse resolution. This finding hasn't been reported previously. The border area between stroma and BM (Fig. 6(D)), as observed in the co-polarized image, shows a more homogenous magenta color tone. This finding is in accordance with previous reports that specify the posterior boundary of BM to usually be barely visible or invisible in co-polarized images [41]. Thus, the magenta color tone actually resembles the very first stromal structures posterior to the BM that do not appear in conventional OCT. The anterior BM (Fig. 6(E)) shows a greenish/whitish tone of color, indicating that both polarization channels contribute to this layer (even if the co-polarized channel dominates). This finding is not quite in accordance to previous reports that claimed BM to be polarization preserving [39]. However, the BM consists of randomly oriented collagen fibrils that could potentially introduce alterations of the incoming polarization state. Finally, the SBP image shows a green color tone (Fig. 6(F)). Even though, visual evidence of subbasal nerve structures can be found in the cross-polarized image (indicating birefringent properties of these fibers), the co-polarized image presents considerably higher image contrast in this layer. This finding suggests that the additional polarization contrast of PS-OCT does not seem to provide additional value for visualizing subbasal nerves.

Before our approach of corneal (PS-) µOCT may be advanced towards human imaging *in vivo* in the future, some technological shortcomings still need to be addressed. Foremost, anticipated subject motion in axial direction will require an increased DOF in order to maintain the layers of interest within the confocal gate. Sacrificing transverse resolution by using a lower NA objective is not an option, due to the small diameter subbasal nerves that still need to be resolved. Multiple promising approaches – software [42] and hardware [43–45] – that enable reasonable DOF

extension while maintaining transverse resolution have been presented to date. However, future investigations are needed to further push the current boundaries of extended DOF technologies so that they are compatible with corneal imaging. The use of a tailored focusing plane that potentially fits the natural curvature of BM might ease the requirements on the respective DOF extension method [24].

Another means for mitigating subject motion is increasing imaging speed. Faster high-resolution line cameras will aid here. However, higher imaging speeds in OCT decrease the signal-to-noise ratio (SNR), which is an issue for supercontinuum source powered OCT instruments that generally operate far from the shot-noise limit, mostly due to increased relative intensity noise (RIN) [46]. The SNR also scales with the illumination power on the sample, which is limited for corneal exposure by the American National Standards Institute (ANSI) laser safety standards and needs to be decreased considerably from the >10 mW used in this study.

The need for a more clinically convenient alternative to IVCM will continue to push OCT research efforts on corneal nerve imaging. The giant pool of ophthalmic [3] and non-ophthalmic [5–7] neurodegenerative diseases will continue to create an imperative for early diagnosis of incipient denervation through corneal imaging.

5. Conclusion

In summary, we have presented morphologic imaging results of excised swine and non-human primate corneas recorded with our close to isotropic resolution µOCT prototype. Cellular and nerval structural features were visualized at resolutions and image quality approaching those of IVCM, at an extended FOV. In particular, subbasal innervation in the SBP was investigated using custom segmentation and tracking algorithms as well as immunohistochemical validation. Furthermore, the incorporation of polarization sensitive contrast enabled corneal PS-OCT at currently unprecedented imaging resolutions.

Disclosures

G.J.T. has a financial/fiduciary interest in SpectraWave, a company developing an OCT-NIRS intracoronary imaging system and catheter. His financial/fiduciary interest was reviewed and is managed by the Massachusetts General Hospital and Partners HealthCare in accordance with their conflict of interest policies. G.J.T. also consults for SpectraWave and receives µOCT sponsored research funding from Vertex, CNUSA Biotech Holdings, Astra Zeneca, Translate Bio, and WayVector.

References

1. L. J. Müller, C. F. Marfurt, F. Kruse, and T. M. T. Tervo, "Corneal nerves: structure, contents and function," Exp. Eye Res. **76**(5), 521–542 (2003).
2. L. Oliveira-Soto and N. Efron, "Morphology of corneal nerves using confocal microscopy," Cornea **20**(4), 374–384 (2001).
3. B. S. Shaheen, M. Bakir, and S. Jain, "Corneal nerves in health and disease," Surv. Ophthalmol. **59**(3), 263–285 (2014).
4. J. He, N. G. Bazan, and H. E. P. Bazan, "Mapping the entire human corneal nerve architecture," Exp. Eye Res. **91**(4), 513–523 (2010).
5. R. A. Malik, P. Kallinikos, C. A. Abbott, C. H. M. van Schie, P. Morgan, N. Efron, and A. J. M. Boulton, "Corneal confocal microscopy: a non-invasive surrogate of nerve fibre damage and repair in diabetic patients," Diabetologia **46**(5), 683–688 (2003).
6. M. Tavakoli, A. Marshall, L. Thompson, M. Kenny, S. Waldek, N. Efron, and R. A. Malik, "Corneal confocal microscopy: A novel noninvasive means to diagnose neuropathy in patients with fabry disease," Muscle Nerve **40**(6), 976–984 (2009).
7. L. Kass-Iliyya, S. Javed, D. Gosal, C. Kobylecki, A. Marshall, I. N. Petropoulos, G. Ponirakis, M. Tavakoli, M. Ferdousi, K. R. Chaudhuri, M. Jeziorska, R. A. Malik, and M. A. Silverdale, "Small fiber neuropathy in Parkinson's disease: A clinical, pathological and corneal confocal microscopy study," Parkinsonism Relat. D. **21**(12), 1454–1460 (2015).
8. L. J. Muller, L. Pels, and G. F. Vrensen, "Ultrastructural organization of human corneal nerves," Invest. Ophthalmol. Vis. Sci. **37**, 476–488 (1996).
9. L. J. Muller, G. F. Vrensen, L. Pels, B. N. Cardozo, and B. Willekens, "Architecture of human corneal nerves," Invest. Ophthalmol. Vis. Sci. **38**, 985–994 (1997).
10. K. Tervo, T. Tervo, L. Eränkö, A. Vannas, A. C. Cuello, and O. Eränkö, "Substance P-immunoreactive nerves in the human cornea and iris," Invest. Ophthalmol. Vis. Sci. **23**, 671–674 (1982).
11. C. F. Marfurt, C. J. Murphy, and J. L. Florczak, "Morphology and Neurochemistry of Canine Corneal Innervation," Invest. Ophthalmol. Vis. Sci. **42**, 2242–2251 (2001).
12. I. Jalbert, F. Stapleton, E. Papas, D. F. Sweeney, and M. Coroneo, "In vivo confocal microscopy of the human cornea," Br. J. Ophthalmol. **87**(2), 225–236 (2003).
13. R. F. Guthoff, A. Zhivov, and O. Stachs, "In vivo confocal microscopy, an inner vision of the cornea - a major review," Clin. Exp. Ophthalmol. **37**(1), 100–117 (2009).
14. S. Bohn, K. Sperlich, S. Allgeier, A. Bartschat, R. Prakasam, K.-M. Reichert, H. Stolz, R. Guthoff, R. Mikut, B. Köhler, and O. Stachs, "Cellular in vivo 3D imaging of the cornea by confocal laser scanning microscopy," Biomed. Opt. Express **9**(6), 2511–2525 (2018).
15. T. D. Weber and J. Mertz, "In vivo corneal and lenticular microscopy with asymmetric fundus retroillumination," Biomed. Opt. Express **11**(6), 3263–3273 (2020).
16. V. Mazlin, P. Xiao, E. Dalimier, K. Grieve, K. Irsch, J.-A. Sahel, M. Fink, and A. C. Boccara, "In vivo high resolution human corneal imaging using full-field optical coherence tomography," Biomed. Opt. Express **9**(2), 557–568 (2018).
17. B. Tan, Z. Hosseinaee, L. Han, O. Kralj, L. Sorbara, and K. Bizheva, "250 kHz, 1.5 um resolution SD-OCT for in-vivo cellular imaging of the human cornea," Biomed. Opt. Express **9**(12), 6569–6583 (2018).
18. Z. Hosseinaee, B. Tan, O. Kralj, L. Han, A. Wong, L. Sorbara, and K. Bizheva, "Fully automated corneal nerve segmentation algorithm for corneal nerves analysis from UHR-OCT images," Proc. SPIE **10858**, 1085823 (2019).
19. W. Drexler, U. Morgner, R. K. Ghanta, F. X. Kärtner, J. S. Schuman, and J. G. Fujimoto, "Ultrahigh-resolution ophthalmic optical coherence tomography," Nat. Med. **7**(4), 502–507 (2001).
20. X. Yao, K. Devarajan, R. M. Werkmeister, V. A. dos Santos, M. Ang, A. Kuo, D. W. K. Wong, J. Chua, B. Tan, V. A. Barathi, and L. Schmetterer, "In vivo corneal endothelium imaging using ultrahigh resolution OCT," Biomed. Opt. Express **10**(11), 5675–5686 (2019).
21. K. Bizheva, B. Tan, B. MacLelan, O. Kralj, M. Hajialamdari, D. Hileeto, and L. Sorbara, "Sub-micrometer axial resolution OCT for in-vivo imaging of the cellular structure of healthy and keratoconic human corneas," Biomed. Opt. Express **8**(2), 800–812 (2017).
22. A. Dubois, L. Vabre, A.-C. Boccara, and E. Beaurepaire, "High-resolution full-field optical coherence tomography with a Linnik microscope," Appl. Opt. **41**(4), 805–812 (2002).
23. V. Mazlin, P. Xiao, J. Scholler, K. Irsch, K. Grieve, M. Fink, and A. C. Boccara, "Real-time non-contact cellular imaging and angiography of human cornea and limbus with common-path full-field/SD OCT," Nat. Commun. **11**(1), 1868 (2020).
24. V. Mazlin, K. Irsch, M. Paques, J.-A. Sahel, M. Fink, and C. A. Boccara, "Curved-field optical coherence tomography: large-field imaging of human corneal cells and nerves," Optica **7**(8), 872–880 (2020).
25. E. Auksorius, D. Borycki, P. Stremplewski, K. Liżewski, S. Tomczewski, P. Niedźwiedziuk, B. L. Sikorski, and M. Wojtkowski, "In vivo imaging of the human cornea with high-speed and high-resolution Fourier-domain full-field optical coherence tomography," Biomed. Opt. Express **11**(5), 2849–2865 (2020).
26. L. Liu, J. A. Gardecki, S. K. Nadkarni, J. D. Toussaint, Y. Yagi, B. E. Bouma, and G. J. Tearney, "Imaging the subcellular structure of human coronary atherosclerosis using micro-optical coherence tomography," Nat. Med. **17**(8), 1010–1014 (2011).

27. S. Chen, X. Liu, N. Wang, X. Wang, Q. Xiong, E. Bo, X. Yu, S. Chen, and L. Liu, "Visualizing Micro-anatomical Structures of the Posterior Cornea with Micro-optical Coherence Tomography," Sci. Rep. **7**(1), 10752 (2017).

28. L. Wang, Q. Xiong, X. Ge, E. Bo, J. Xie, X. Liu, X. Yu, X. Wang, N. Wang, S. Chen, X. Wu, and L. Liu, "Cellular resolution corneal imaging with extended imaging range," Opt. Express **27**(2), 1298–1309 (2019).

29. P. Tankam, Z. He, G. Thuret, H. B. Hindman, C. Canavesi, J. C. Escudero, T. Lépine, P. Gain, and J. P. Rolland, "Capabilities of Gabor-domain optical coherence microscopy for the assessment of corneal disease," J. Biomed. Opt. **24**(04), 046002 (2019).

30. C. Canavesi, A. Cogliati, A. Mietus, Y. Qi, J. Schallek, J. P. Rolland, and H. B. Hindman, "In vivo imaging of corneal nerves and cellular structures in mice with Gabor-domain optical coherence microscopy," Biomed. Opt. Express **11**(2), 711–724 (2020).

31. J. F. de Boer, C. K. Hitzenberger, and Y. Yasuno, "Polarization sensitive optical coherence tomography - a review [Invited]," Biomed. Opt. Express **8**(3), 1838–1873 (2017).

32. C. Hitzenberger, E. Goetzinger, M. Sticker, M. Pircher, and A. Fercher, "Measurement and imaging of birefringence and optic axis orientation by phase resolved polarization sensitive optical coherence tomography," Opt. Express **9**(13), 780–790 (2001).

33. Y. Jung, J. H. Ng, C. P. Keating, P. Senthil-Kumar, J. Zhao, M. A. Randolph, J. M. Winograd, and C. L. Evans, "Comprehensive Evaluation of Peripheral Nerve Regeneration in the Acute Healing Phase Using Tissue Clearing and Optical Microscopy in a Rodent Model," PLoS One **9**(4), e94054 (2014).

34. C. Elhardt, C. M. Wertheimer, A. Wartak, J. Zhao, H. M. Leung, S. A. Kassumeh, B. Yin, G. J. Tearney, and R. Birngruber, "Stromal Nerve Imaging and Tracking Using Micro-Optical Coherence Tomography," Trans. Vis. Sci. Tech. **9**(5), 6 (2020).

35. P. P. Srinivasan, S. J. Heflin, J. A. Izatt, V. Y. Arshavsky, and S. Farsiu, "Automatic segmentation of up to ten layer boundaries in SD-OCT images of the mouse retina with and without missing layers due to pathology," Biomed. Opt. Express **5**(2), 348–365 (2014).

36. C. A. Schneider, W. S. Rasband, and K. W. Eliceiri, "NIH Image to ImageJ: 25 years of image analysis," Nat. Methods **9**(7), 671–675 (2012).

37. E. Meijering, M. Jacob, J.-C. F. Sarria, P. Steiner, H. Hirling, and M. Unser, "Design and validation of a tool for neurite tracing and analysis in fluorescence microscopy images," Cytometry **58A**(2), 167–176 (2004).

38. M. Pircher, C. K. Hitzenberger, and U. Schmidt-Erfurth, "Polarization sensitive optical coherence tomography in the human eye," Prog. Retinal Eye Res. **30**(6), 431–451 (2011).

39. F. Beer, A. Wartak, R. Haindl, M. Gröschl, B. Baumann, M. Pircher, and C. K. Hitzenberger, "Conical scan pattern for enhanced visualization of the human cornea using polarization-sensitive OCT," Biomed. Opt. Express **8**(6), 2906–2923 (2017).

40. E. Götzinger, M. Pircher, M. Sticker, A. Fercher, and C. Hitzenberger, "Measurement and imaging of birefringent properties of the human cornea with phase-resolved, polarization-sensitive optical coherence tomography," J. Biomed. Opt. **9**(1), 94–102 (2004).

41. F. Beer, A. Wartak, N. Pircher, S. Holzer, J. Lammer, G. Schmidinger, B. Baumann, M. Pircher, and C. K. Hitzenberger, "Mapping of Corneal Layer Thicknesses With Polarization-Sensitive Optical Coherence Tomography Using a Conical Scan Pattern," Invest. Ophthalmol. Vis. Sci. **59**(13), 5579–5588 (2018).

42. Y.-Z. Liu, F. A. South, Y. Xu, P. S. Carney, and S. A. Boppart, "Computational optical coherence tomography [Invited]," Biomed. Opt. Express **8**(3), 1549–1574 (2017).

43. Z. Ding, H. Ren, Y. Zhao, J. S. Nelson, and Z. Chen, "High-resolution optical coherence tomography over a large depth range with an axicon lens," Opt. Lett. **27**(4), 243–245 (2002).

44. L. Liu, C. Liu, W. C. Howe, C. J. R. Sheppard, and N. Chen, "Binary-phase spatial filter for real-time swept-source optical coherence microscopy," Opt. Lett. **32**(16), 2375–2377 (2007).

45. B. Yin, K. K. Chu, C.-P. Liang, K. Singh, R. Reddy, and G. J. Tearney, "µOCT imaging using depth of focus extension by self-imaging wavefront division in a common-path fiber optic probe," Opt. Express **24**(5), 5555–5564 (2016).

46. R. D. Engelsholm and O. Bang, "Supercontinuum noise reduction by fiber undertapering," Opt. Express **27**(7), 10320–10331 (2019).